Heat transfer enhancement by chaotic advection in a novel sine-helical channel geometry

Abbas Aldor, Yann Moguen, Kamal El Omari, Charbel Habchi, Pierre-Henri Cocquet, Yves Le Guer

Heat transfer enhancement by chaotic advection in a novel sine-helical channel geometry

Abbas Aldor[a,b], Yann Moguen[a], Kamal El Omari[c], Charbel Habchi[b], Pierre-Henri Cocquet[a], Yves Le Guer[a,*]

[a] *Université de Pau et des Pays de l'Adour, E2S-UPPA, SIAME, Pau, France*
[b] *Notre Dame University-Louaize, Thermofluids Research Group, Zouk Mosbeh, Lebanon*
[c] *University of Reunion Island, PIMENT laboratory, 40 Av. Soweto, Saint-Pierre, 97455, La Réunion, France*

Abstract

In this paper, we present an innovative sine-helical heat exchanger whose channel geometry consists in a combination of a helically coiled geometry and a sine-wave geometry. Laminar flow is considered in the present study, with the Reynolds numbers ranging from 100 to 1400. The flow structure and the convective heat transfer in the novel heat exchanger are analyzed numerically using the finite volume method. The results are compared to those obtained with a classical helically coiled heat exchanger. It is shown that the periodic change of the centrifugal forces in the sine-helical channel breaks the flow symmetry and leads to chaotic particle trajectories.

The effect of chaotic advection on the enhancement of mixing efficiency is evidenced. The coefficient of variation of the outlet temperature in the sine-helical flow is decreased by about 100 % relative to that in the helical channel, highlighting thus a better temperature homogeneity. Moreover, the thermal enhancement factor, measuring the convective heat transfer coefficient at same pumping power, is also increased between 5.5 and 20.7% in the since-helical flow relative to the helical channel. Consequently, the proposed novel heat exchanger is very promising for many applications with laminar flow regimes.

Keywords: sine-helical flow; chaotic advection; heat transfer enhancement; streamwise vortices; OpenFoam.

1. Introduction

Enhancement of the heat transfer in multifunctional heat exchangers/reactors has attracted a lot of attention over the past decades. One of the passive methods to improve the convective heat transfer within a fluid is to modify the parietal surfaces to generate complex flow structure. Among the existing solutions, most of them use curved channels which are now ubiquitous in the industrial operations thanks to their wide range of applications in heat transfer, chemical reaction, filtration, separation or dispersion (see [70] for a detailed review).

In curved pipes and channels, the centrifugal forces lead to the generation of a secondary flow structure consisting of counter-rotating streamwise vortices often called Dean cells [48, 35, 71]. The pioneering theoretical analysis of the generation of such 2−vortex flows was conducted by Dean, for fully developed flows in an infinitely long curved pipe of circular cross-section with small constant curvature [21], and between two concentric cylinders with small constant curvature [22]. It was found that flows in curved pipes and channels depend primarily on a single dimensionless number called the Dean number. In the expression of the Dean number, denoted by De, two dimensionless parameters appear: *(1)* the curvature ratio of the channel, which is also, in physical terms, the ratio

*Corresponding author. Tel.: +33 5 59 40 71 63.
Email address: yves.leguer@univ-pau.fr (Yves Le Guer)

Nomenclature

$\boldsymbol{v}$	Velocity (m/s)
ΔP	Pressure drop (Pa)
a	Square cross-section length (m)
c	Constant coefficient (-)
c_p	Thermal capacity ($J\ kg^{-1}K^{-1}$)
D_h	Hydraulic diameter (m)
De	Dean number (–)
f	Friction factor (-)
H	Helicity ($m\ s^{-2}$)
h	Heat transfer coefficient ($W\ m^{-2}\ K^{-1}$)
k_f	Fluid thermal conductivity ($W\ m^{-1}\ K^{-1}$)
l	Parametrized channel length (m)
M	Number of revolutions of the curve (-)
Nu	Nusselt number (–)
P	Pressure (Pa)
p	Pitch of helix (m)
Pr	Prandtl number (–)
R	Radius of helix (m)
Re	Reynolds number (–)
T	Temperature (K)

Abbreviations

CoV	Coefficient of variation
$LMTD$	logarithmic mean temperature difference

Greek symbols

α	Thermal diffusivity ($m^2\ s^{-1}$)
ϵ	Local curvature (–)
η	Thermal enhancement factor (–)
κ	Curvature of the curve (-)
λ	Local ratio of torsion to curvature (–)
μ	Dynamic viscosity (Pa s)
ρ	Mass density ($kg\ m^{-3}$)
σ_T	Standard deviation of temperature (K)
τ	Torsion of the curve (-)

Subscripts

s	Straight channel
w	Wall
$inlet$	Heat exchanger inlet
$outlet$	Heat exchanger outlet
m	Mean value
$cell$	Element of the mesh

of the centrifugal force to the viscous force and *(2)* the Reynolds number based on the average axial flow velocity [75, 10]. The Dean number reads:

$$\mathrm{De} = \mathrm{Re}\sqrt{\frac{D_h}{R}}, \tag{1}$$

where Re is the Reynolds number, D_h is the hydraulic diameter of the channel cross-section and R is the radius of the curvature of the convex surface of the curved channel.

A flow instability, termed the Dean instability, may develop beyond a critical value of De, and additional pairs of vortices appear near the concave wall [72, 9, 27]. At an even larger Dean number, a 6− cell flow may be observed, with two pairs of Dean vortices [52]. The appearance of unstable Dean vortices is observed for various cross-sections [55], where the values of De at which transition occurs depend on the shape of the cross-section. In the present study, a square cross-section is considered since it allows a heat transfer better than for circular cross-section, mainly because a square duct has higher surface-to-volume ratio [58].

From the widely used curved channels, the helical ones are the most utilized. This is due to their efficient mixing even at low Reynolds number their compactness in structure, and ease of manufacture, all with a small increase in pressure drop. Helical coiled pipe flows are used in many applications such as static mixers [35, 36, 51], heat exchangers [19, 73] [49] and chemical reactors

[41, 39]. Numerous studies, as *e.g.* those above cited, focus on the enhancement of the heat and mass transfer phenomena in these devices owing to their good performances with relatively low power consumption.
Meanwhile, the symmetric ordered flow structure in helically coiled flow and the relatively low streamwise circulation power limit their ability to achieve high rates of convective heat transfer. Thus, many studies are conducted in order to break the flow order and generate chaotic advection [4, 56, 5]. Chaotic advection is a mechanism that, in laminar flows, allows the generation of complex trajectories of fluid particles which then facilitate mixing [5, 67]. In 2D plane flows, to generate chaotic advection, it is necessary that the velocity field is time dependent. In 3D flows, on the other hand, the additional degree of freedom brought by the third dimension does not impose this constraint of unsteadiness of the flow. In a conventional helical channel with a uniform low curvature, the streamlines represented in the cross-section always have the same pattern, they trap the fluid between them, which does not allow the transport of material perpendicular to these streamlines frozen in space. This is no longer the case in a channel that has varying curvature and/or torsion in the direction of flow, the streamlines shown in consecutive cross-sections evolve, allowing the fluid paths to sample the entire cross-section and thus facilitate mixing and parietal heat transfer in the case of a heat exchanger.

Chaotic advection has significant advantages in enhancing the heat transfer process with low additional power consumption [44, 53, 35, 19]. This could be done for instance by using a continuously twisted channel flow [40, 15], multiple S-type bends [16] or joined pipes of differing helical radius in a series configuration [17]. Thus, by twisting two consecutive portions of the channel, the separatrix between the Dean cells may be broken. Complex trajectories and chaotic advection of particles [4, 5, 67] are then obtained, as shown numerically by Jones *et al.* in [40], and experimentally by Le Guer and Peerhossaini in [44]. Numerous studies have then proven the effectiveness of this geometry with twisted curved channels to improve mixing [12, 45, 35, 7, 77, 28, 26], heat transfer [59, 53, 13, 1, 14, 46, 76] or reactive transfer [11]. Table 1 below summarizes important and most recent works in the domain of chaotic heat exchangers and mixers.

In the present study, the novel sine-helical heat exchanger is presented. It is designed as a channel geometry whose generating curve can be considered as a superimposition of a sine curve on a helical curve whose modulations are in the axial direction of the helix. Such a chaotic exchanger can be of interest for several applications, including those used to process fragile or temperature-sensitive viscous products, such as food, biological or chemical products [19], and also for laminar flow mixing applications such as those encountered in the chemical and pharmaceutical industries [63]. The objective of the present work is to analyze numerically the flow patterns and heat transfer in this novel sine-helical flow and to compare its thermal efficiency to those obtained for more conventional channel flows in a helical duct and straight duct.

	Work technique	Explanation	Conditions	Application
Peerhossaini *et al.* 1993 [59]	Experimental	Twisted curved channel	$328 < \mathrm{Re} < 1243$	Heat transfer Hydrodynamic flow Mixing
Yamagishi *et al.* 2007 [74]	Numerical	Multiple pipe bends composed of 90-bends	$220 < \mathrm{Re} < 1790$	Heat transfer Fluid flow
Kumar *et al.* 2007 [43]	Experimental study	Coiled flow inverter	$1000 < \mathrm{Re} < 16000$	Heat transfer
Zheng *et al.* 2013 [78]	Numerical	Periodic square cross-sections zigzag channels	$50 < \mathrm{Re} < 400$	Heat transfer Fluid flow
Zheng *et al.* 2013 [79]	Numerical	Periodic zigzag semicircular channels	$50 < \mathrm{Re} < 320$	Heat transfer Fluid flow
Garg *et al.* 2015 [30]	Analytical	Circlet and serpentine microchannels	$\mathrm{Re} < 25$	Mixing
Creyssels *et al.* 2015 [18]	Numerical and experimental	Multi-level laminating mixer (MLLM)	$10 < \mathrm{Re} < 3000$	Heat transfer Mixing
Tohidi *et al.* 2015 [69]	Numerical	Multiple pipe bends composed of 90-bends	$100 < \mathrm{Re} < 500$	Heat transfer Fluid flow
Shi *et al.* 2019 [66]	Numerical Experimental	Zigzag millimetric channels	Laminar flow	Heat transfer
Bahrani *et al.* 2019 [8]	Experimental	Chaotic laminar mixer CLM	$100 < \mathrm{Re} < 2000$	Heat transfer
Dbouk *et al.* 2019 [20]	Numerical	Chaotic twisted pipes	$50 < \mathrm{Re} < 150$	Mixing
Reddy *et al.* 2020 [61]	Numerical	Novel curved serpentine coil	$500 < \mathrm{Re} < 2000$	Fluid flow Heat transfer
Mansour *et al.* 2020 [51]	Numerical study	Coiled flow reverser (CFR)	$10 < \mathrm{Re} < 3000$ $10 < \mathrm{Re} < 3000$	Mixing Heat transfer
Cui *et al.* 2020 [19]	Numerical	A circle-arc-wavy helically coiled pipe heat exchanger (CAWC)	$\mathrm{Re} = 200, 400,$ $800, 1600, 3200$	Mixing Heat transfer
Awasthi *et al.* 2021 [6]	Numerical	Curved serpentine coil	$500 < \mathrm{Re} < 2000$	Heat transfer Fluid flow

Table 1: list of the previous numerical and experimental works in the field of enhancement of heat transfer and mixing due to chaotic advection

Incompressible Newtonian laminar flows with Reynolds number ranging from 100 to 1400 are considered in this work. These values of the Reynolds number are lower than the critical one for sustained turbulence in straight pipe. They are thus also lower than the critical value for a flow in curved pipes since the curvature stabilizes the flow which thus increases the critical value of the Reynolds number [3, 42]. The Navier-Stokes and energy equations governing the fluid flow and heat transfer in the channels are thus solved without using any turbulence model.

The paper is organized as follows: In Section 2, we present the computational domain for the new sine-helical channel flow with the mathematical formulation of the generating curve. Section 3 is devoted to the governing equations and the definition of the different performance parameters used to compare the sine-helical channel with helical and straight channels. The results on flow structure and heat transfer enhancement are discussed in Section 4, and concluding remarks and perspectives are finally given in Section 5.

2. Computational domains and non-dimensional parameters

The channel geometries considered in the present study are obtained following the principle of parallel curves (see *e.g.* [24]). This can be obtained by calculating the normal vector at each point of the curve defined by the fundamental curve, to construct 4 daughter parallel curves that are equidistant from the fundamental curve, and by ensuring that no twist will occur along the path. This method of construction will make the tangent vector of the fundamental curve at any point be the normal of the cross-section formed by the 4 points corresponding to the 4 daughter curves at the same point. This building technique is clarified in Figure 1 which also clearly shows the difference between the parallel curves and offset curves in 2D.

The sine-helical fundamental curve can be seen as a superimposition of an oscillating curve on a standard helix, parameterized as

$$\gamma(R;\theta) = \left\{ \begin{array}{lcl} x(\theta) & = & R\cos(\theta), \\ y(\theta) & = & R\sin(\theta), \\ z(\theta) & = & p\theta + cR\sin(b\theta), \end{array} \right. \tag{2}$$

where R is the radius of the helix, p is the vertical step or pitch, c is a coefficient associated with the amplitude of the sine oscillations and b is related to the period Θ of the sine-function by $b = 2\pi/\Theta$. The number of revolutions of the sine-helical curve is designated by $M_{\rm sh}$ which is related to θ as

$$0 \leqslant \theta \leqslant 2\pi M_{\rm sh}. \tag{3}$$

The parametrization of the generating sine-helical curve is denoted by $\gamma(R;\theta)$ as defined in (2). Its unit tangent vector $\vec{T}(R;\theta) = \partial_\theta \gamma(R;\theta)$ is

$$\vec{T}(R;\theta) = \frac{1}{\sqrt{f(R;\theta)}} \begin{pmatrix} -R\sin(\theta) \\ R\cos(\theta) \\ p + cRb\cos(b\theta) \end{pmatrix}, \quad f(R;\theta) = R^2 + [p + cRb\cos(b\theta)]^2.$$

A unit normal vector can then be calculated as

$$\vec{N}(R;\theta) = \frac{1}{\sqrt{f(R;\theta)}} \begin{pmatrix} [cRb\cos(b\theta) + p]\sin(\theta) \\ -[cRb\cos(b\theta) + p]\cos(\theta) \\ R \end{pmatrix}.$$

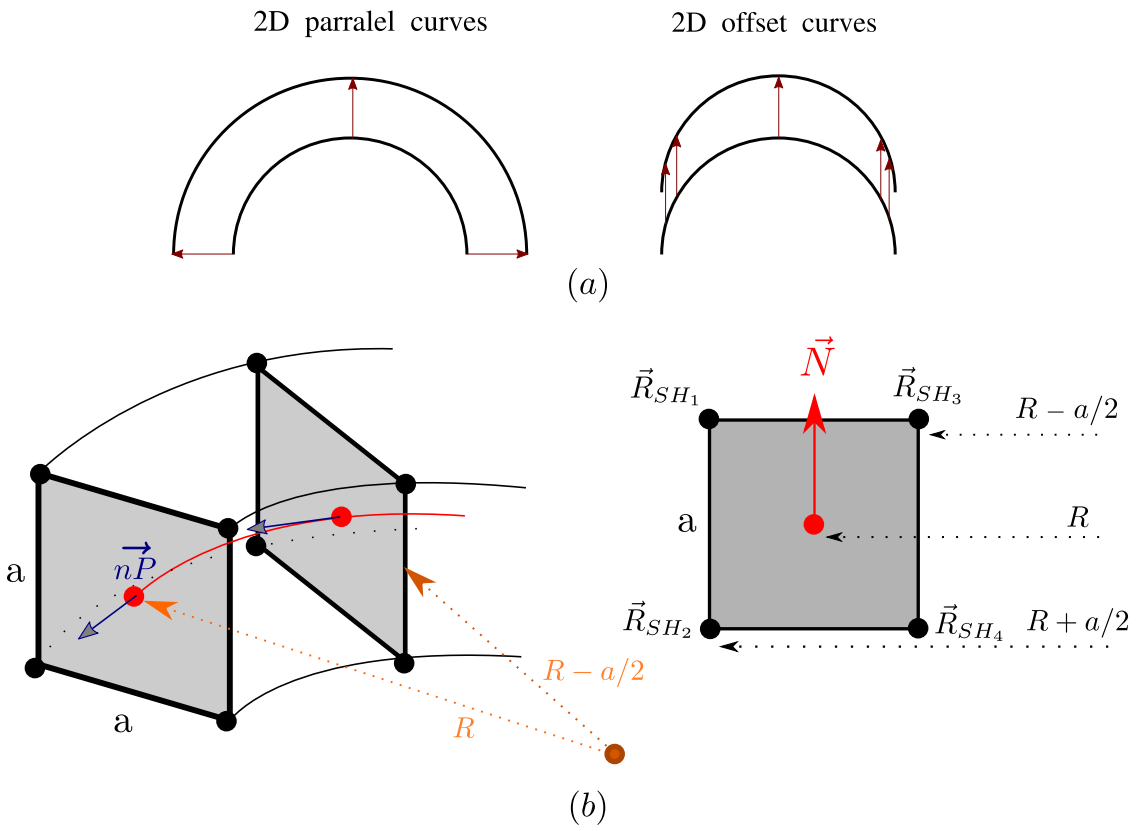

Figure 1: (a) Difference between parallel curves and offset curves principle in 2D, and (b) explanation of how the fundamental curve is the normal of the plane formed by 4 daughter curves constructed following the principle of parallel curves.

As discussed above, we now parametrize four other curves (namely the daugther curves) as follows:

$$\begin{aligned}
R_{SH_1}(\theta) &= \gamma\left(R+\frac{a}{2};\theta\right) + \frac{a}{2}\vec{N}\left(R+\frac{a}{2};\theta\right),\\
R_{SH_2}(\theta) &= \gamma\left(R+\frac{a}{2};\theta\right) - \frac{a}{2}\vec{N}\left(R+\frac{a}{2};\theta\right),\\
R_{SH_3}(\theta) &= \gamma\left(R-\frac{a}{2};\theta\right) + \frac{a}{2}\vec{N}\left(R-\frac{a}{2};\theta\right),\\
R_{SH_4}(\theta) &= \gamma\left(R-\frac{a}{2};\theta\right) - \frac{a}{2}\vec{N}\left(R-\frac{a}{2};\theta\right).
\end{aligned} \tag{4}$$

These four curves are shown in Figure 1. The helical fundamental curve, with its 4 daughter helical parallel curves are also considered in the following. They are parametrized by Eqs. (2) and (4), by taking $c = 0$ (or equivalently with $b = 0$), with $0 \leqslant \theta \leqslant 2\pi M_\mathrm{h}$, where M_h is the number of revolutions that was chosen to equalize the length of the fundamental helical curve with that of the sine-helical one.

To compare the thermal and mixing performances of the channels corresponding to the previously described geometries, the generating curves must have the same length. For a parametrized curves $\gamma : \eta \in [a, b] \mapsto (x(\eta), y(\eta), z(\eta)) \in \mathbb{R}^3$, its length is

$$l = \int_a^b \sqrt{\dot{x}(\eta)^2 + \dot{y}(\eta)^2 + \dot{z}(\eta)^2}\,\mathrm{d}\eta. \tag{5}$$

For the sine-helical channel, this is

$$l_{\mathrm{sine-helical}} = \int_0^{2\pi M_{\mathrm{sh}}} \sqrt{cRb\cos(b\theta)\left[cRb\cos(b\theta)+2p\right]+R^2+p^2}\,\mathrm{d}\theta. \tag{6}$$

The length of the helical channel is obtained by setting either $c = 0$ or $b = 0$ in (6) and is then

$$l_{\mathrm{helical}} = 2\pi M_{\mathrm{h}}\sqrt{R^2+p^2}. \tag{7}$$

With $M_{\mathrm{sh}} = 2$ for the sine-helical channel, $M_{\mathrm{h}} = 2.631$ for the helical channel, the two generating curves have the same length $l = 66.5a$. Here and from now on, a is the length of the side of the square cross-section of the channels. The shapes of the two channels built according to the method described in Figure 1 that are studied in this paper are shown in Figure 2. In addition

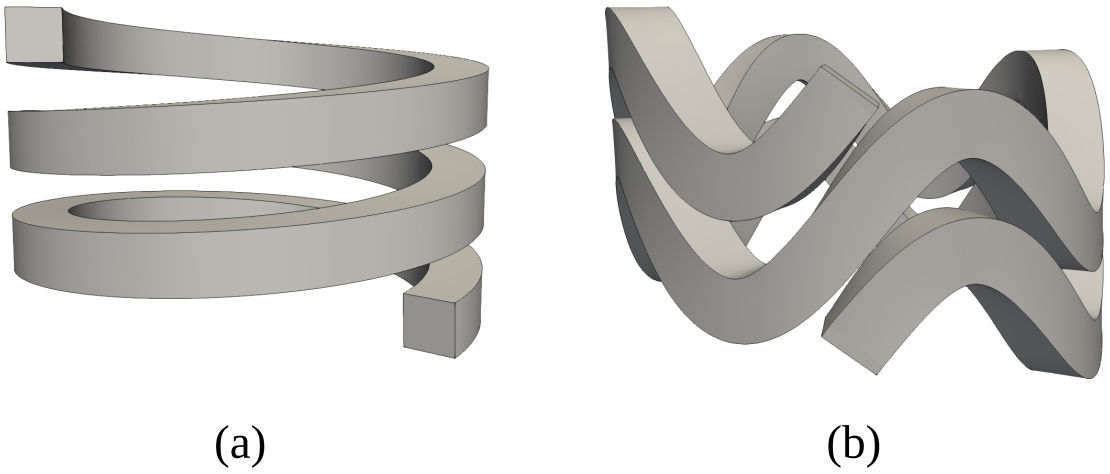

Figure 2: (a) The helical, and (b) the sine-helical channels, with the same square cross-section and the same length, $l = 66.5a$. The parameters of the generating curves are: $R = 4a$, $p = 0.3a$, $b = 4$, $c = 5/16$, or $c = 0$ for the helical channel.

to the helical and sine-helical channels, we are also going to consider a straight channel with the same length.

Useful dimensionless numbers have been studied by Germano [31, 32] for flows in channels with constant curvature and torsion. However, in the case of the sine-helical channel, both curvature and torsion depend on the θ-angle. In order to identify relevant dimensionless parameters common for the two channel geometries, we rather follow Gammack and Hydon [29], who studied the effects of non-constant curvature and torsion on flows in pipes. Adapted to our geometries and notations, the dimensionless parameters considered by these authors are

$$\mathrm{Re} = \frac{U_0 a}{\nu}, \quad \varepsilon(\hat{\theta}) = a\kappa(\theta), \quad \lambda(\hat{\theta}) = \frac{\tau(\theta)}{\kappa(\theta)}, \quad \text{where} \quad \hat{\theta} = \frac{\theta}{a}, \tag{8}$$

where κ is the curvature, τ the torsion and U_0 the cross-sectionally averaged velocity as the curvature tends to zero. ε is the local curvature parameter and λ is the local ratio of torsion to curvature.

For the sine-helical channel, the curvature and torsion are

$$\kappa(\theta) = \frac{\sqrt{-\left\{c^2b^4R^2[\cos(b\theta)]^2-[\cos(b\theta)]^2R^2b^2c^2-c^2b^4R^2-2\cos(b\theta)Rbcp-R^2-p^2\right\}R^2}}{\left\{[\cos(b\theta)]^2R^2b^2c^2+2\cos(b\theta)Rbcp+R^2+p^2\right\}^{3/2}}, \tag{9}$$

$$\tau(\theta) = \frac{cRb^3\cos(b\theta) - cRb\cos(b\theta) - p}{c^2b^4R^2[\cos(b\theta)]^2 - [\cos(b\theta)]^2R^2b^2c^2 - c^2b^4R^2 - 2\cos(b\theta)Rbcp - R^2 - p^2}. \tag{10}$$

Note that κ and τ are periodic in variable θ with period $\Theta = 2\pi/b$. Due to the complex dependence of these functions on the geometrical channel parameters, we will only use numerically computed maximum values of the functions ε, which is non-negative, and $|\lambda|$:

$$\varepsilon_{\text{sine-helical}} = \max \varepsilon(\hat{\theta}),\ \ \lambda_{\text{sine-helical}} = \max \left|\lambda(\hat{\theta})\right|. \tag{11}$$

For the helical channel, the curvature and torsion are $\kappa = R/(R^2+p^2)$ and $\tau = p/(R^2+p^2)$, and the dimensionless parameters are

$$\varepsilon_{\text{helical}} = \frac{aR}{R^2+p^2},\quad \lambda_{\text{helical}} = \frac{p}{R}. \tag{12}$$

Note that with $p = 0$ in the expression of $\varepsilon_{\text{helical}}$, the curvature a/R that enters in the Dean number expression $\text{De} = \text{Re}\sqrt{a/R}$ for the flow in a curved pipe [21, 22] is retrieved. More generally,

$$\varepsilon_{\text{helical}} = \left(\frac{\text{De}}{\text{Re}}\right)^2 \frac{1}{1+p^2/R^2}.$$

In addition, note that the expressions of $\varepsilon_{\text{helical}}$ and λ_{helical} for the helical geometry are retrieved if the sine-helical geometry reduces to the helical one, *i.e.* in the special case of $c = 0$ or $b = 0$.

For the parameter values considered in the sequel of this study, namely

$$\begin{array}{l} a = 1 \text{ cm},\ \ R = 4a,\ \ p = 0.3a,\ \ b = 4, \\ c = \frac{5}{16}\ \ \text{(sine-helical channel)}\ \ \text{or}\ \ \ c = 0\ \ \ \text{(helical channel)}, \end{array} \tag{13}$$

the obtained dimensionless curvature and ratio of torsion to curvature are

$$\begin{array}{ll} \varepsilon_{\text{helical}} = 0.2486, & \lambda_{\text{helical}} = 0.075, \\ \varepsilon_{\text{sine-helical}} = 1.264, & \lambda_{\text{sine-helical}} = 18.825. \end{array} \tag{14}$$

The dimensionless parameters from (8) are plotted in Figure 3.

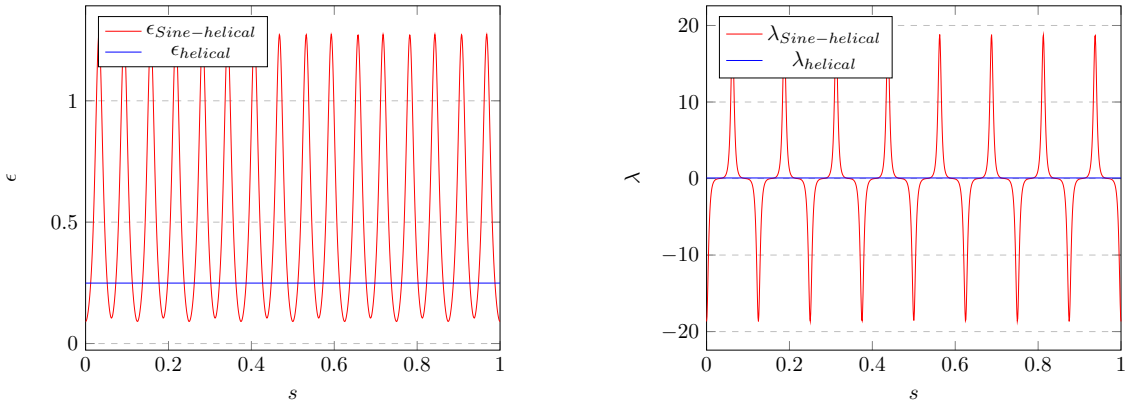

Figure 3: The dimensionless parameters ε, (a), and λ, (b), for the sine-helical and the helical geometries. To compare them, the parameters are rescaled as function of $s = 2\pi M/\hat{\theta} \in [0,1]$, where $M = M_{\text{sh}} = 2$ for the sine-helical channel.

Using parameters (14), the (dimensionless) torsion of the helix is

$$a\tau_{\text{helical}} = \lambda_{\text{helical}}\varepsilon_{\text{helical}} \approx 0.018.$$

Note that ε can be written as $\varepsilon = a\kappa(\theta) = a/r(\theta)$ where $r(\theta)$ is the (local) radius of curvature. For the helical channel studied below, this gives $\varepsilon_{\text{helical}} \approx 0.24$. We recall that the Dean vortices are solutions to the incompressible Navier-Stokes equation obtained when retaining only the leading order for small dimensionless curvature, namely $\varepsilon \ll 1$. As a result, in our study, we do not expect Dean vortices to appear in the helical channel since $\varepsilon_{\text{helical}}$ is not small enough even if the torsion effects on the flow may be negligible. Owning to (14) and Figure 3, the parameters controlling the flow in the sine-helical channel are function of $\hat{\theta}$ while they are constant for the helical channel. Therefore, the sine-helical channel is going to exhibit complex flows compared to the helical channel. This will be confirmed in the sequel by numerical simulations.

3. Governing equations and research method

3.1. Governing equations

We consider incompressible flows of a Newtonian viscous fluid with heat transfer. The fluid is water and the flows are laminar, with the bulk Reynolds number Re defined in Eq. (8) ranging from 100 to 1 400. The conservation equations for mass, momentum and energy, according to [54] are

$$\nabla \cdot \boldsymbol{v} = 0, \tag{15}$$

$$\partial_t \boldsymbol{v} + (\boldsymbol{v} \cdot \nabla)\boldsymbol{v} = -\frac{1}{\varrho}\nabla p + \nu \nabla^2 \boldsymbol{v}, \tag{16}$$

$$\partial_t T + \nabla \cdot (\boldsymbol{v} T) = \alpha \nabla^2 T, \tag{17}$$

where ϱ, $\boldsymbol{v}$, p and T are the density, the velocity, the pressure and the temperature; ν is the kinematic viscosity and α is the thermal diffusivity (see Table 2).

3.2. Boundary conditions

For the three channels considered in the present study, a fully developed velocity profile is imposed at the inlet. According to Delplace [23], considering the origin of the Cartesian coordinates y and z at the centre of the square cross-section (zy plane), the velocity field of the fully established laminar flow of a Newtonian liquid is such that

$$v_x(y,z) = \frac{16(\Delta P)a^2}{\nu L \pi^3} \sum_{n=1,3,5,..}^{\infty} \frac{(-1)^{\frac{n-1}{2}}}{n^3} \left[1 - \left(\frac{\cosh\left(\frac{n\pi y}{2a}\right)}{\cosh\left(\frac{n\pi}{2}\right)}\right)\right] \cos\left(\frac{n\pi z}{a}\right), \tag{18}$$

where l is the pipe length, a is the length of the side of the square cross-section, and the pressure drop ΔP can be calculated from the desired average velocity v_{avg}, using

$$v_{\text{avg}} = \frac{32(\Delta P)a^2}{\nu L \pi^4} \sum_{n=1,3,5,...}^{\infty} \frac{1}{n^4} \left[1 - \frac{2}{n\pi}\tanh\left(\frac{n\pi}{2}\right)\right]. \tag{19}$$

At the outlet, the gradient velocity is set to zero. The no-slip condition is applied at the wall. The same constant temperature is imposed along the wall, with $T_{\text{wall}} = T_{\max} = 323$ K. At the inlet, the temperature value is fixed, with $T_{\text{inlet}} = T_{\min} = 293$ K. At the outlet, the temperature gradient is set to zero.

Density (ϱ)	1 000 kg m^{-3}
Dynamic viscosity ($\mu = \varrho\nu$)	10^{-3} Pa s
Specific heat (c_p)	4 207.1 W kg^{-1}K^{-1}
Thermal diffusivity (α)	1.4×10^{-7} m^2 s^{-1}

Table 2: Fluid properties.

3.3. Numerical schemes

We use the open source code OpenFOAM [38]. The numerical method is thus based on a finite-volume formulation with co-located variable arrangement (for details on the schemes and algorithms mentioned below, the interested reader is referred *e.g.* to [54]). First, to verify that the studied flows are steady, simulations were done using the icoFoam solver of OpenFoam, devoted to incompressible unsteady flows. Thus, the governing equations above listed are solved with their transient terms. We have adapted the icoFoam solver in order to compute the temperature equation using the velocity field obtained from the continuity and momentum equations. The time integration is done with a combination of the Crank-Nicolson and the Euler implicit schemes, allowing both suitable level of accuracy and positivity enforcement. At each time-step, the pressure and velocity fields are calculated with the PISO algorithm. The interpolation of pressure and temperature at the cell faces is linear. The convection terms are discretized using the upwind scheme. The diffusion term is discretized by a second-order accurate scheme using Gauss linear corrected scheme.

After having verified that the considered flows are steady, we conducted the simulations with the steady simpleFoam solver, which uses the SIMPLE algorithm in its steady version. The governing equations are then solved without the transient terms, which allows an important gain in computation time. The interpolation of the pressure and the temperature, and the discretization of the convection terms and the diffusion terms are the same as for the simulations with the transient terms.

3.4. Grid generation and mesh sensitivity analysis

The three considered channels have the same length (see section 2). The meshes were generated using Gmsh [33], using hexahedral elements, with a special attention paid to the near-wall refinement to carefully compute the velocity and temperature field in this region with high gradients (see Fig. 4). Simulations of the most complex geometry, namely the Sine-Helical channel, were conducted for the highest Reynolds number $Re = 1400$ with several mesh densities and refined until the relative difference between the values of the resulting overall Nusselt number for two consecutive mesh densities did not exceed 2%, which is satisfactory according to recommendation based on the GCI [62] algorithm as shown in table 3 . Finally, the mesh size is approximately the same for all the considered geometries, with about 9×10^6 cells for the finest mesh.

	Mesh Size	grid size (mm)	N_u
coarse	1350646	0.37	43.8
medium	3856006	0.26	41.6
Fine	9550566	0.19	40.7
extrapolated value		40.28	
GCI		1.3 %	
order of convergence		4	

Table 3: GCI analysis based on the Nusselt number and mesh size for the sine-helical channel.

3.5. Performance indicators for mixing and thermal exchanges

To compare the heat transfer efficiency in the different channel geometries, we consider widely used mixing indicators that can be monitored along the channels. The first one is the mean temperature of the fluid in a cross-section, which represents the energy extracted from the wall:

$$T_{\mathrm{m}} = \frac{1}{\sum_{\mathrm{cross-section}} A_{\mathrm{cell}} U_{\mathrm{cell}}} \left(\sum_{\mathrm{cross-section}} A_{\mathrm{cell}} U_{\mathrm{cell}} T_{\mathrm{cell}} \right) \tag{20}$$

where the summation is over the cells of the cross-section under consideration, and A_{cell} and U_{cell} denotes the area and mean flow velocity of the intersection of a 3-D cell and of the cross-section respectively.

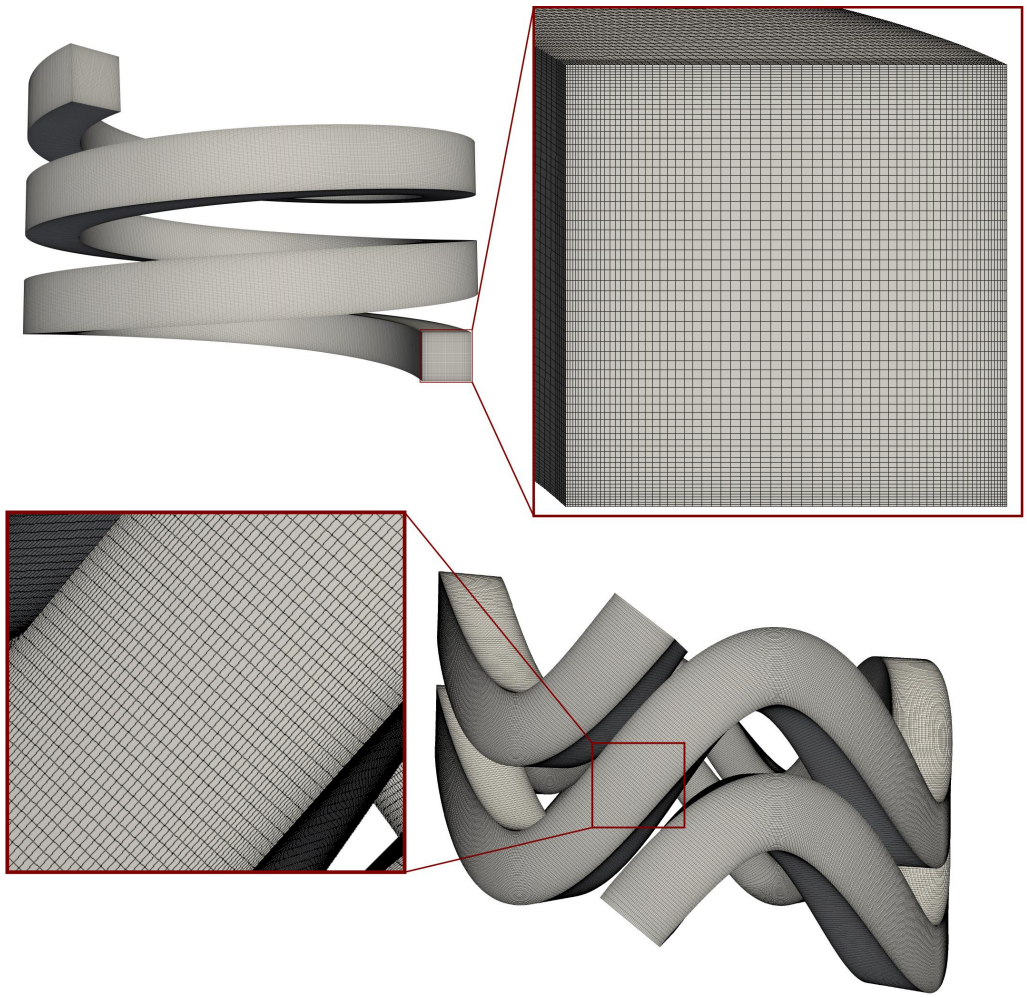

Figure 4: Meshes of the sine-helical and helical channels with 8×10^6 cells.

Another useful indicator is the standard deviation of the fluid temperature inside a cross-section, which represents the level of homogenization of the temperature:

$$\sigma_T = \left[\frac{1}{\sum_{\text{cross-section}} A_{\text{cell}}} \sum_{\text{cross-section}} A_{\text{cell}} \left(T_{\text{cell}} - T_{\text{m}}\right)^2 \right]^{1/2}. \tag{21}$$

The coefficient of variation of the fluid temperature is then defined as the ratio of the standard deviation to the mean temperature:

$$\text{CoV}_T = \frac{\sigma_T}{T_m}. \tag{22}$$

We also examine the overall Nusselt number, which characterizes the parietal heat transfer along a channel:

$$\text{Nu}_{\text{m}} = \frac{1}{l} \int_0^l \text{Nu}(s)\, \text{d}s, \tag{23}$$

where l is the length of the generating curve of the channel (see section 2), and Nu - defined in (24) - is the local Nusselt number expressed with the duct hydraulic diameter, which is equal to the side length a of the square cross-section in our case:

$$\text{Nu} = \frac{ha}{k_f}, \tag{24}$$

where h is the heat transfer coefficient calculated from the wall heat flux density Q and LMTD such that $h = Q/\text{LMTD}$, with LMTD the logarithmic mean temperature difference between the inlet and the outlet of a channel defined as :

$$\text{LMTD} = \frac{T_{\text{outlet}} - T_{\text{inlet}}}{\log\left(\dfrac{T_{\text{wall}} - T_{\text{inlet}}}{T_{\text{wall}} - T_{\text{outlet}}}\right)}. \tag{25}$$

We can define also the friction factor f that represents the pressure losses and defined as:

$$f = \frac{2a\Delta p}{\rho l V_{\text{inlet}}^2}, \tag{26}$$

where Δp is the pressure difference between the inlet and the outlet and V_{inlet} is the average velocity at the inlet.

To express the enhancement in heat transfer with the consideration of the pressure drop penalty, we can define the thermohydraulic enhancement factor η according to Webb and Eckert [80] given as

$$\eta = \frac{\text{Nu}}{\text{Nu}_s} \frac{f_s}{f}^{1/3}, \tag{27}$$

where the index "s" refers to results corresponding to the straight channel.

4. Results and discussion

4.1. Validation of the CFD model for straight and helical channels

In order to assess the accuracy of the used CFD solver, we have conducted hydrodynamic and thermal simulations for carefully chosen test cases. The thermal simulations were compared to well-known correlations given for heat transfer and friction factor.

First, we conducted a numerical simulation for a hydrodynamic flow in a 180° bent channel, a generic geometry which presents secondary flows in the transverse plane of the channel. The results obtained have been compared with the experimental ones of Hille *et al.* [37] for the same geometry. The difference between the results is satisfactory (1.9 % difference on the maximum velocity).

Then, we conducted a simulation for laminar thermally and hydrodynamically fully developed flow

in a straight duct with square cross-section for a constant wall temperature. Results showed that the local Nusselt number at the outlet of the channel was Nu = 3.01 which was in good agreement with the literature (Nu = 2.976) [57].
Furthermore, we conducted a simulation for developing laminar flow inside a straight duct of square section, with constant wall temperature boundary condition also. Friction factor extracted from CFD results was plotted in figure 5, and compared to results from the correlation of Shah and London [65], given by the equation :

$$f = \frac{56.9}{\mathrm{Re}}. \tag{28}$$

Figure 5 showed that our results are in good agreement with this correlation.

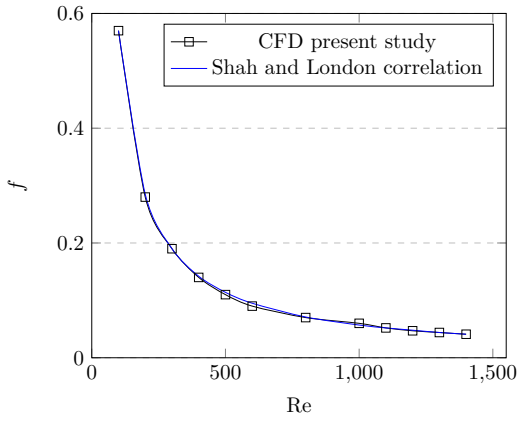

Figure 5: Comparison of calculated friction factor for the straight pipe with developing laminar flow to that for Shah and London [65].

Another tested application was the classical helical channel for which we made a comparison for both Nusselt number and friction factor for a wide range of Reynolds number to well established correlations. For Nusselt number comparison, we took correlations of Schmidt [64] and Acharya *et al.* [2] which are summarized in table 4.
For the friction factor comparison, we took correlations of Manlapaz and Churchill [50], Srinivasan *et al.* [68] and Prandtl [60] which are summarized in Table 5. It can be seen in Figure 6 that our numerical results are in good agreement with these correlations for the evaluation of the Nusselt number or the friction factor f, even for the higher considered values of the Reynolds number.

References	$\mathrm{Nu_m}$ correlations	Conditions
Schmidt [64]	$3.65 + 0.08\left[1 + 0.8\left(\frac{a}{2R}\right)^{0.9}\right]\mathrm{Pr}^{1/3}\,\mathrm{Re}^{0.5+0.2903\left(\frac{a}{2R}\right)^{0.194}}$	$100 < \mathrm{Re} < \mathrm{Re}_c$
Acharyia *et al.* [2]	$0.676\left(\frac{a}{R}\right)^{0.13}\mathrm{Re}^{0.5}\,\mathrm{Pr}^{0.21}$	$\mathrm{Pr} > 1$

Table 4: Nusselt number correlations for helical channels with constant wall temperature. Re_c is the critical Reynolds number for transition to turbulent flow.

References	f/f_s correlations	Conditions
Manlapaz and Churchill [50]	$\sqrt{1+\left(1+\frac{a/R}{3}\right)^2\left(\frac{\mathrm{De}}{88.33}\right)}$	$\mathrm{De} > 40$
Srinivasan *et al.* [68]	$0.419\ \mathrm{De}^{0.275}$ $0.1125\ \mathrm{De}^{0.5}$	$30 < \mathrm{De} < 300$ $\mathrm{De} > 300$
Prandtl [60]	$0.29\ \mathrm{De}^{0.36}$	$\mathrm{De} > 40$

Table 5: Friction factor correlations for helical channels. f_s is the friction factor for straight channel.

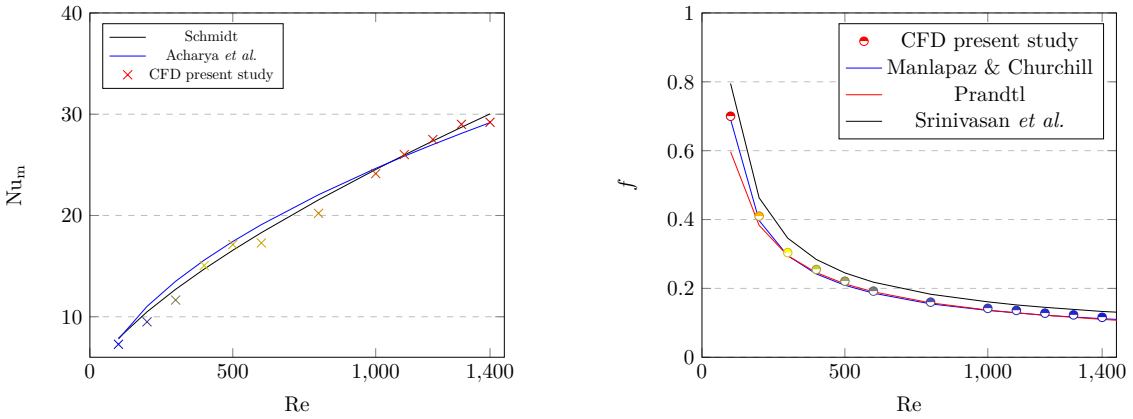

Figure 6: Nusselt Number (left) and friction factor (right) correlations for the helical channel, compared to the CFD results of the present study, as functions of the Reynolds number.

4.2. Flow structure and temperature distribution

In order to compare the flow and temperature fields in the helical and sine-helical channel configurations, the secondary velocity fields and temperature fields were presented at the outlet of the channel for the two configurations.

For better data visualization and to facilitate the analysis of the results, we define the local coordinates system (x', y', z') as shown in Figure 7. These coordinates are always directed relatively to the active channel cross-section, such that x' is always directed to the outer lateral wall of the channel and y' is always directing to the upper curved wall of the channel, both together (x', y') establish a plane that is always perpendicular to the generating parametrized curve (see Eqs. (2)), and z' is always indicating the streamwise direction. Hence, V_x' and V_y' represent the spanwise velocity components, and $V_{z'}$ is the streamwise component of the velocity vector in the new coordinates system (x', y', z').

The graphical representation of the vorticity, which is the curl of the velocity field, $\nabla \times \boldsymbol{v}$, is not the most appropriate approach here, because the vorticity generated by the presence of the walls hinders the representation of the vortices far from the walls. For this reason, we prefer to consider the helicity:

$$H = \boldsymbol{v} \cdot \nabla \times \boldsymbol{v}.$$

The helicity filters out the regions with low vorticity, as well as regions of high vorticity but with low speed where the angle between the velocity and vorticity vectors is large (such as in the boundary layer). By this way, we can differentiate between primary and secondary vortices [47]. The helicity can be positive or negative, which signifies the direction of swirl of the vortex

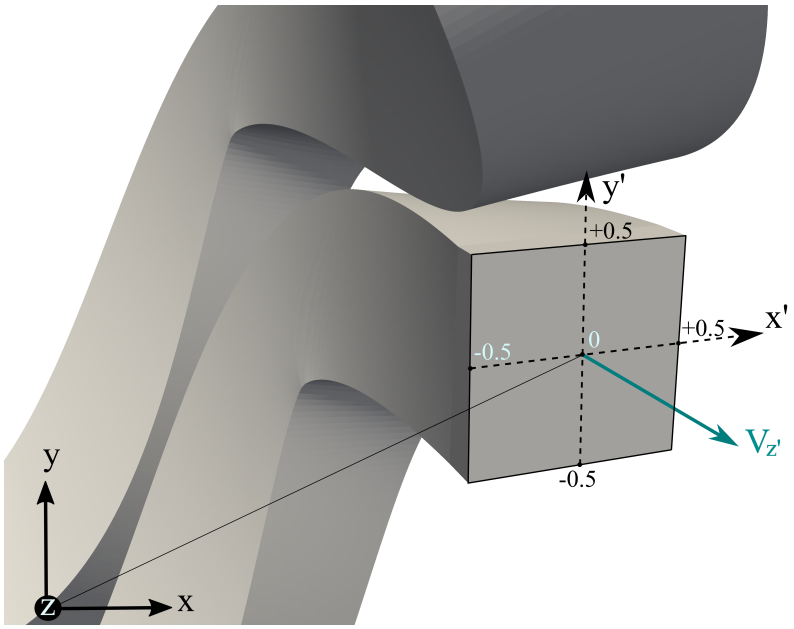

Figure 7: Coordinate systems in a cross-section plane.

relative to the streamwise velocity, For positive values, it indicates anti-clockwise rotation where negative values present clockwise rotation. In Figures 8 and 9, a vertical slice cuts the two channels vertically in their middle. It cuts the sine-helical channel in 4 cross-sections, each far from the inlet by a non-dimensional distance $\bar{l}$, and all are given as $\bar{l} = \{0.15625, 0.40625, 0.65625, 0.90625\}$, where the last value ($\bar{l} = 0.90625$) corresponds to the magnified sine-helical cross-section. The vertical slice cuts the helical channel in 6 cross-sections, that are far from the inlet by distances $\bar{l} = \{0, 0.19, 0.38, 0.57, 0.76, 0.95\}$, where the last value ($\bar{l} = 0.95$) corresponds to the magnified helical cross-section. In Figure 8, the contours of the helicity were shown at different cross-sections. In the helical channel, the development of two Dean cells is clear, where two horizontal cores of helicity with quite the same magnitude but opposite direction are the indicators of the two primary vortices. For the sine-helical channel, the helicity is much more complex which is expected from Figure 3. Indeed, several longitudinal vortex cells coexist and their respective shapes evolve along the channel. This results is due to the continuous evolution of the direction of the centrifugal force along the channel which promotes chaotic advection.

In Figure 9, we see that at different cross sections of the helical channel, better thermal mixing occurs near the outer curved wall, due to the presence of Dean cells. However, the thermal mixing is still limited inside the two main Dean vortices because the core of the vortices are colder.

For the sine-helical channel, the temperature patterns are quite homogeneous at the exit of the channel, which is an indication of good thermal homogenization of the temperature scalar as compared to what happens in the helical channel. This is due to the breaking of the symmetry of those patterns observed in the helical case.

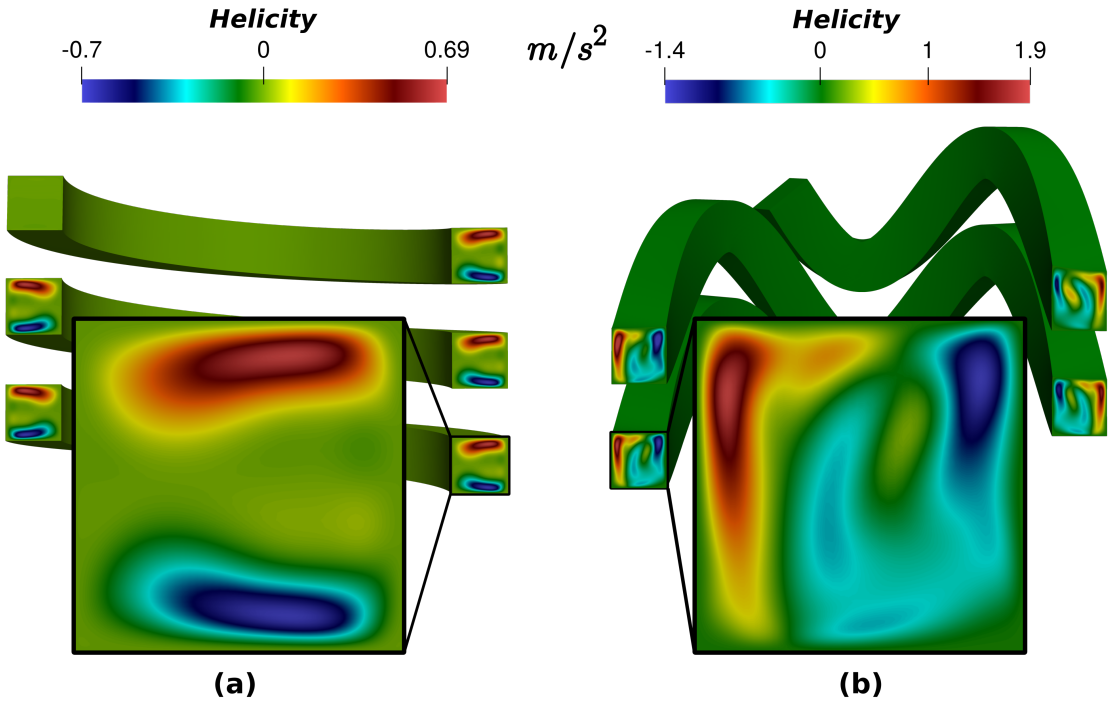

Figure 8: The contours of helicity field components in a vertical slice cutting half the (a) helical channel, and (b) sine-helical channel, for Reynolds number Re = 300. The inlet is the top section.

From Figure 9, we notice first that the isotherms represent the two Deans cells very well and that the homogenization of the fluid at the outlet is much greater in the sine-helical channel. In addition, the temperature at the center is not too far from the wall temperature contrarily to the helical channel for which important temperature gradients subsist in the cross-section at half the channel length.

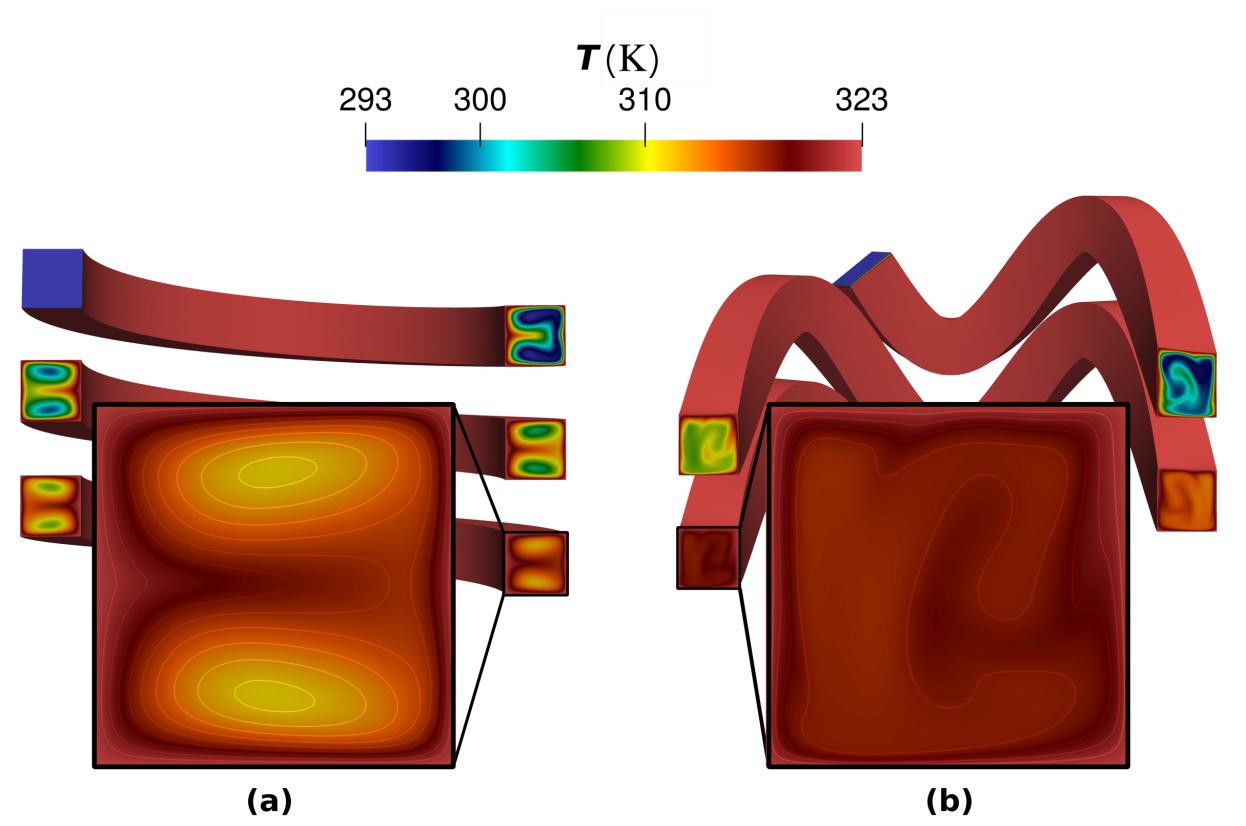

Figure 9: Temperature fields in a vertical slice at half the channel length for, the helical channel (a) and sine-helical channel (b) for Reynolds number Re = 300. The inlet flow is in the top section.

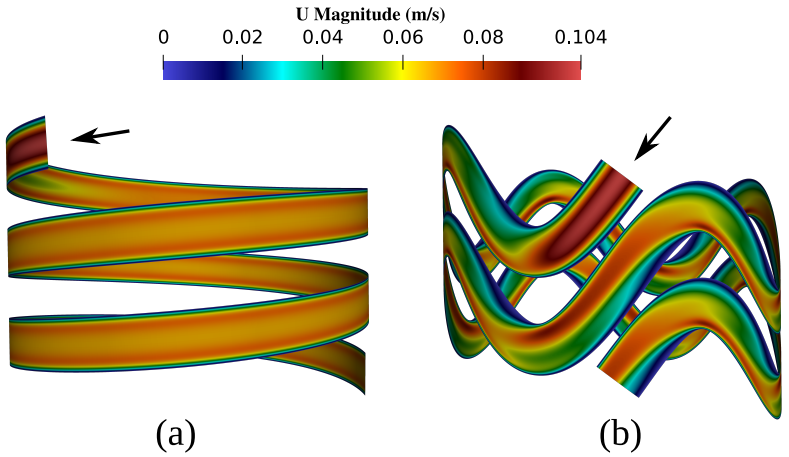

Figure 10: Module of the velocity field in a cylindrical slice coinciding with the curved plane passing through the middle of (a) Helical channel, and (b) Sine-helical channel, for Reynolds number Re = 300. The black arrow indicates the flow direction in each case.

From Figure 10, we observe that the flow reaches rapidly a hydrodynamically fully developed state in the case of the helical configuration. This is not the case for the sine-helical configuration for which the velocity field exhibits a strong periodic modulation along the channel, while the field

appears to be periodic after each revolution .

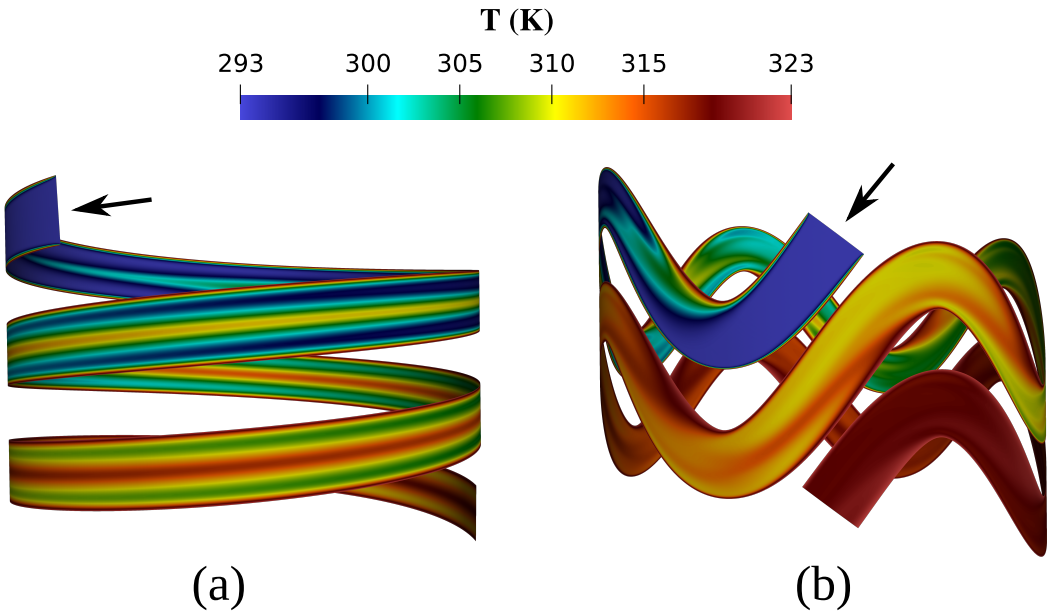

Figure 11: Temperature field in a cylindrical slice coinciding with the curved plane passing through the middle of (a) Helical channel and (b) Sine-helical channel, for Re = 300. The black arrow indicates to the flow direction in each case.

It is clear from Figure 11-(a) that the thermal field reflects the presence of the Dean cells and indicates also their shape preservation along the channel. On the contrary, in the case of the sine-helical channel (see Figure 11-(b)), the thermal field homogenizes rather quickly along the channel. This is due to the continuously variation of the velocity field along the channel.

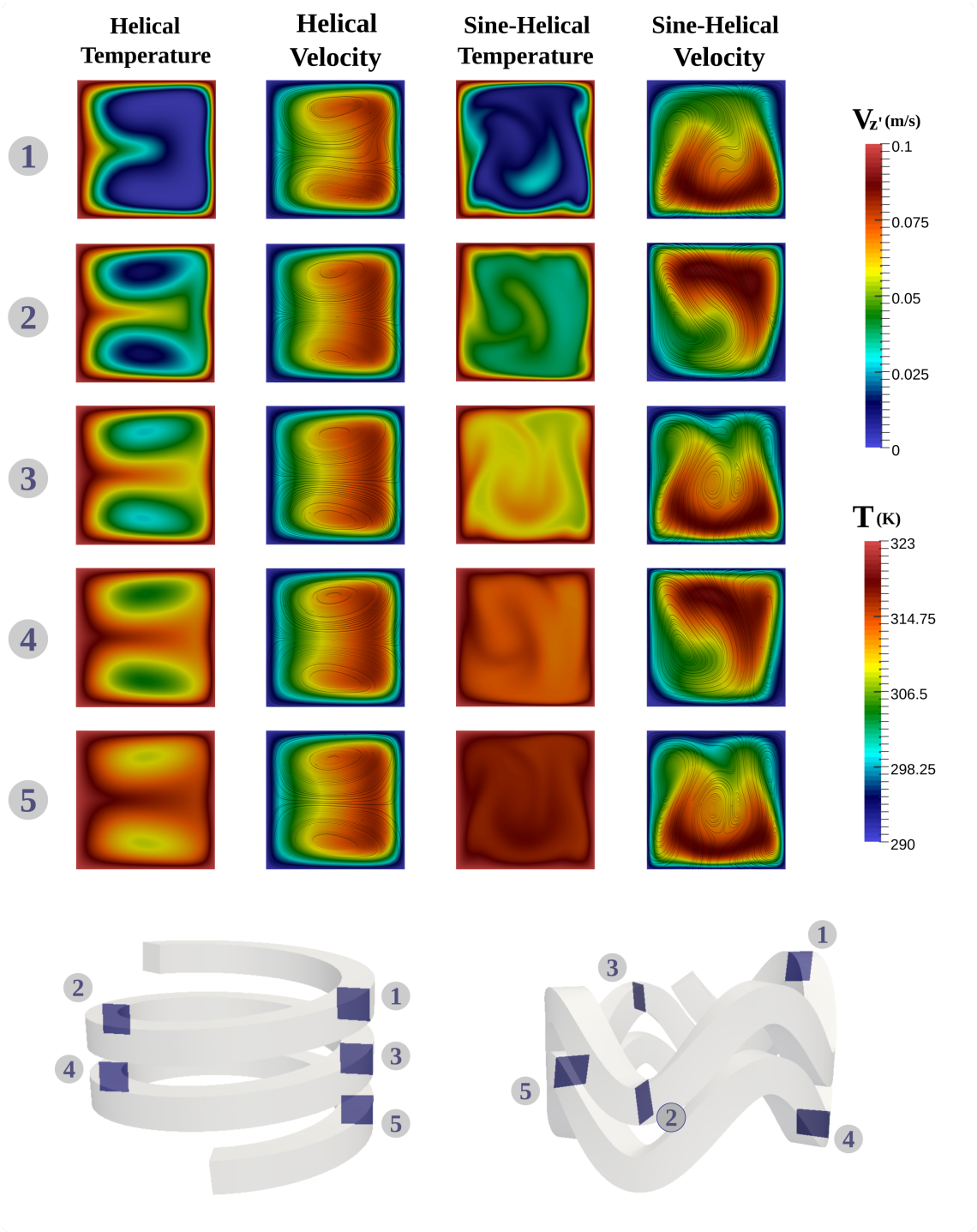

Figure 12: Temperature and velocity fields given in five different cross-sections along the sine-helical and the helical channels and for Re = 300. On the velocity fields plots are superimposed the streamlines of the secondary flow in the cross section. The five cross-section planes were chosen in a way that corresponds to the crests and troughs in the sine-helical case.

Figure 12 presents the developments of the temperature and velocity fields for helical and sine-helical channel at five equidistant streamwise locations, that are far from the inlet by an equal non dimensional distance for the two channels, and given as $\bar{l} = \{0.0935, 0.281, 0.46875, 0.656, 0.8435\}$.

It shows the contours of stream-wise velocity (in addition with surface streamlines of the secondary flow) and temperature at different cross-sections as the fluid moves from the inlet to the outlet of the channel.
For the helical channel we clearly observe the development of the two Dean cells that are steady along the channel.

The temperature patterns (left column) correspond very well to the shapes of the vortex cells and the temperature homogenization is done slowly towards the core of the cells as we move forward in the flow, colder fluid remains trapped inside the two symmetrical vortices. Finally gradients of temperature are still important in the outlet section of the channel.
The much more perturbed transverse flow in the sine-helical channel leads to better mixing and temperature homogenization. This appears well by comparing the temperature contours, and especially at position 5, where the temperature field is quite homogeneous in the whole cross-section. To illustrate this, we can take a look at the streamlines. For the sine-helical channel, from position 1 to 5, as the cross-section planes goes from crest to trough and the reverse, the vortices change their position and shape, leading to a redistribution of the velocities in the different cross-sections. This is the phenomenon which induces the chaotic advection and that ensures the better mixing of the scalar by creation of complex interwoven trajectories. The classical symmetrical cells encountered in the helical channel does not exist in the sine-helical channel for which the curvature and torsion of the canal changes periodically and are not small enough to ensure apparition of the so-called Dean cells.

In order to see the effect of the Reynolds number on the temperature fields, we plot the dimensionless axial temperature profile along the central horizontal and vertical axis of the outlet cross-section ($x = 0$ and $y = 0$) for the sine-helical and the helical channels. They are illustrated in Figure 13 At the right column of this figure is plotted the temperature profile at the vertical axis, and in the case of the helical geometry it shows two peaks with lower temperatures that clearly reflects the presence of the Dean cells, where the temperature acts as a passive tracer. On the contrary, for the sine-helical geometry the temperature profiles are very flat hence indicates a good homogenization. This behavior is also observed along the horizontal axis, *i.e.* the temperature profile in the sine-helical channel is more flat than the one in the helical channel.

4.3. Mixing indicators/coefficients

Figure 14 shows that for the whole studied range of the Reynolds number, Nusselt number for the sine-helical channel was significantly higher than for the straight and helical channels. However, the friction factor was larger in the sine-helical case for all Reynolds range. This can be troublesome for some applications that require low pressure drops. In such a situation it might be useful to attempt to minimise these losses through an optimisation study of the geometrical parameters (amplitudes and wavelengths of sinusoidal disturbances).

The coefficient of variation of the temperature at the outlet section which is an important indicator for the mixing, is shown in Figure 15. The mixing efficiency of the proposed chaotic mixer is clearly evidenced.

In most applications, when designing a heat exchanger, it is not sufficient to study the Nusselt number and ignore the pressure losses. Then, to get a clear global idea about the performance of the exchanger, it is essential to make the comparison of the heat transfer efficiency for both helical and sine-helical exchangers at constant pumping power. For this purpose, we use the thermal enhancement factor η previously defined in 27, which is equivalent to calculate the ratio of the heat exchanger convective heat transfer h to that obtained in a straight-pipe flow h_0 at constant pumping power [34]. Figure 15 shows the enhancement factor relative to a straight channel used as reference. A significant enhancement in the performance is demonstrated by the chaotic heat exchanger for all considered values of the Reynolds number.

As an example, the overall parietal Nusselt number for each of the two configuration of heat exchangers of the same length is given in the table 6 for $\mathrm{Re} = 500$.

For $\mathrm{Re} = 500$, the sine-helical channel configuration gives an increase of the overall Nusselt number of 31.12 % comparing to the helical channel configuration and of 323 % comparing to the straight channel configuration. This already significant increase in the overall Nusselt number will

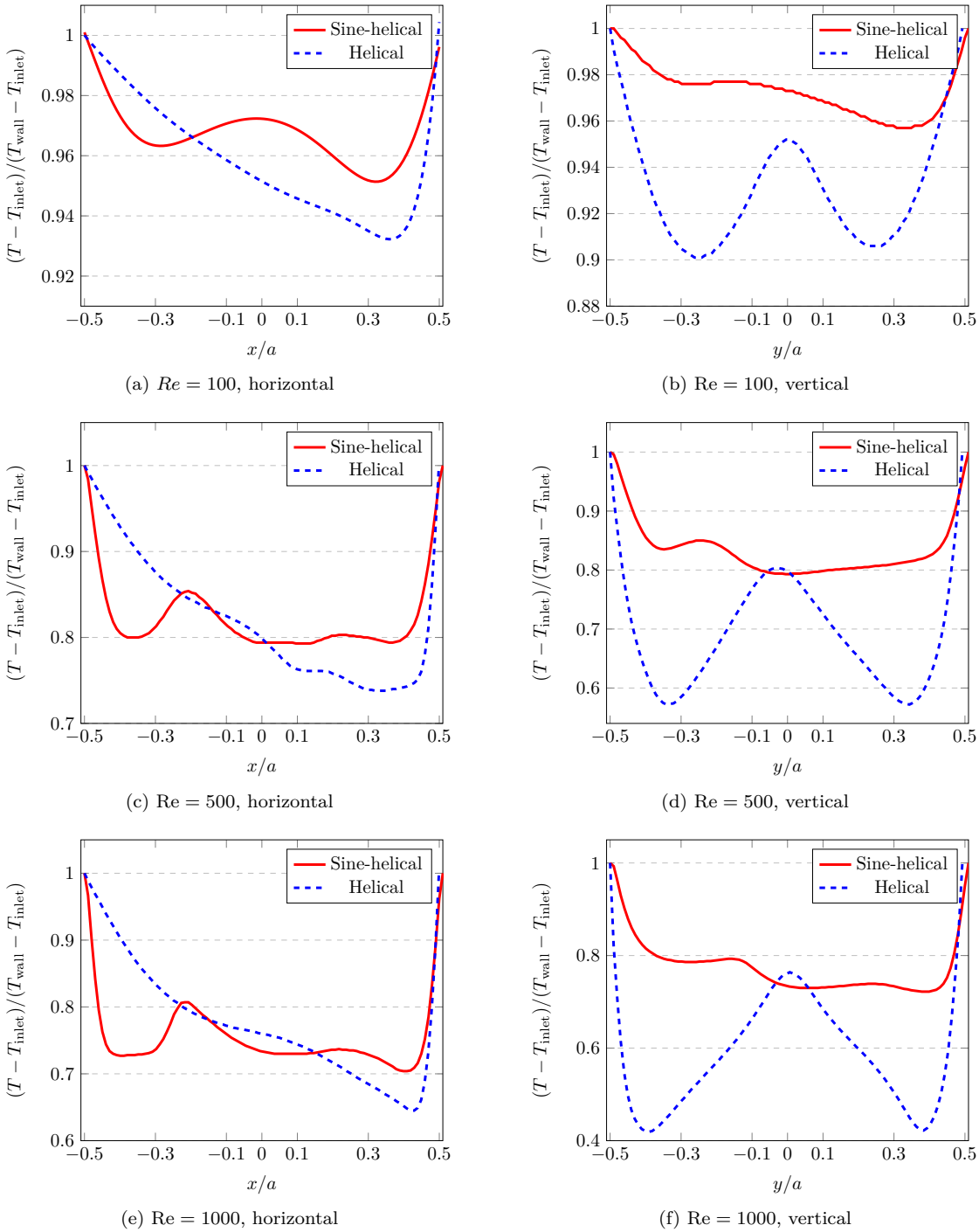

(a) $Re = 100$, horizontal

(b) Re = 100, vertical

(c) Re = 500, horizontal

(d) Re = 500, vertical

(e) Re = 1000, horizontal

(f) Re = 1000, vertical

Figure 13: Dimensionless temperature profiles at outlet center axis (horizontal axis at the left figure and vertical axis at the right figure) for Reynolds number Re = 100, Re = 500 and Re = 1 000 for the sine-helical channel (in red color) and the helical channel (in dashed-blue color). See Fig. 7.

be even greater as the Reynolds number grows up [25]. The sine-helical channel configuration also gives better results in terms of the mean temperature (T_{m} increases) and its homogenization in the cross section (CoV_T decreases), that indicates its efficiency in mixing. However it has the largest friction coefficient. As said above, it will be interesting in a future work, to consider a minimisation

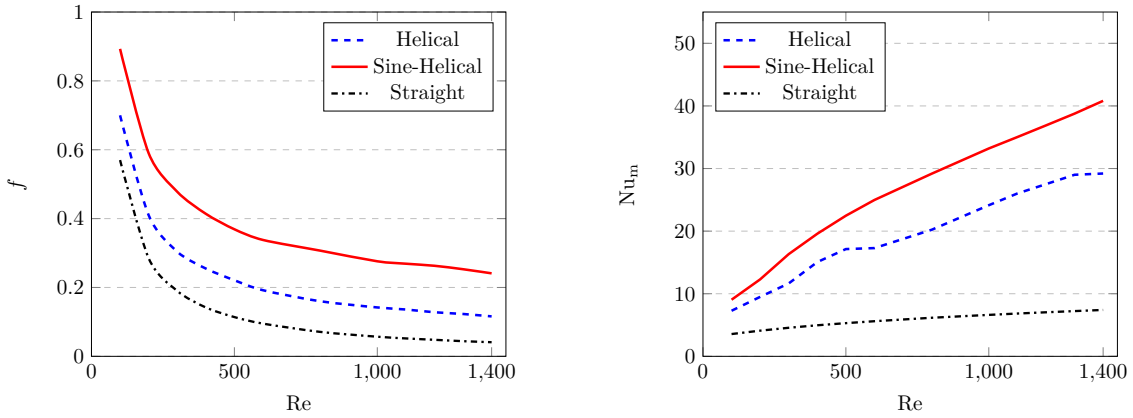

Figure 14: Friction factor f, and Nusselt number $\mathrm{Nu_m}$, as a function of Reynolds number for the three configurations.

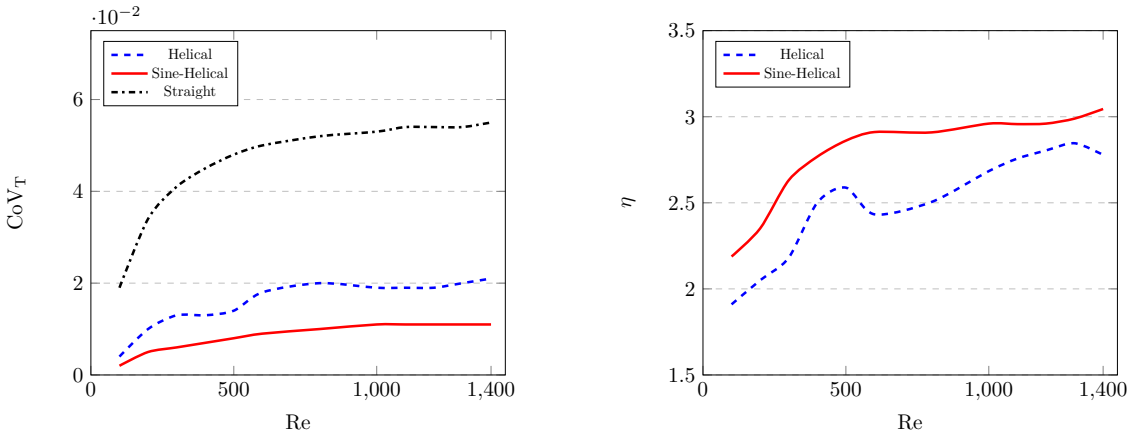

Figure 15: Coefficient of variation of the outlet temperature $\mathrm{CoV_T}$ as a function of Reynolds number for the three configurations. Enhancement factor η as a function of Reynolds number for the sine-helical, and helical channels with respect to the straight channel.

Geometry	T_m	LMTD	σ_T	CoV_T	$\mathrm{Nu_m}$	f
Straight	302.7	24.78	14.45	0.0477	5.303	0.113
Helical	314.6	16.94	4.408	0.0140	17.133	0.221
Sine-helical	317.3	14.54	2.577	0.0081	22.465	0.369

Table 6: Mixing and heat transfer indicators for all geometrical configurations for Reynolds number Re = 500: mean temperature, logarithmic mean temperature difference, variance of temperature, coefficient of variation, mean Nusselt number and friction factor.

of this coefficient by tuning the sine-helical geometry.

5. Conclusions and perspectives

The performance of the novel sine-helical heat exchanger was studied numerically in the laminar regime, and compared to the classical helical one. The results showed that chaotic advection enhanced the mixing and heat transfer inside the sine-helical channel by breaking the Dean cells due to continuous change of the centrifugal force direction. This was noticed qualitatively from the contours of the temperature and velocity fields, and quantitatively from the decrease in the coefficient of variation of the outlet temperature in the sine-helical case by about 100% relative

to that in the helical channel, with increase in the thermal enhancement factor between 5.5 and 20.7% in the since-helical flow relative to the helical channel.

The objective of this work is to propose a novel design for a heat exchanger combining the helically coiled and sine wave geometries. The aim of this first work is to prove the sine-helical heat exchanger effectiveness compared to a more traditional solution commonly used in the industry, namely the helical heat exchanger. A more complete study will be undertaken for the same purpose at different flow regimes in order to better describe the mechanism involved in the increase of mixing and heat transfer. Also, as a future plan, the parametrized geometry will be optimized in order to minimize pressure losses.

This innovative wavy channel geometry (the sine-helical one) is compact and opens new and numerous perspectives for use in areas where heat or mass transfer needs to be more efficient, particularly for applications where mixing is controlled and limited by a diffusion process. Its use as a chemical reactor could also be beneficial, and since it is mathematically parametrized, it offers potential for the search of optimal geometry for the design of innovative and highly efficient mixers, heat exchangers and reactors.

Acknowledgements

The authors would like to acknowledge the National Council for Scientific Research of Lebanon (CNRS-L) and E2S UPPA (Energy and Environment Solutions) for granting a doctoral fellowship to Aldor Abbas.

This research was carried under the framework of E2S UPPA supported by the "Investissements d'Avenir" French programme managed by ANR (ANR-16-IDEX-0002).

It was granted access to the HPC resources of Pyrene (UPPA Cluster, France) and Curta (University of Bordeaux, France).

Pierre-Henri Cocquet is supported by the "Agence Nationale de la Recherche" (ANR), Project O-TO-TT-FU number ANR-19-CE40-0011.

The sine-helical heat exchanger technology presented in this article is the subject of a French patent PCT/FR2020050044 - 01/14/2020 and of an international application WO2020148501 - 07/23/2020.

References

[1] N. Acharya, M. Sen, and H.C. Chang. Heat transfer enhancement in coiled tubes by chaotic advection. *Int. J. Heat Mass Transf.*, 35:2475–2489, 1992.

[2] N. Acharya, M. Sen, and H.C. Chang. Analysis of heat transfer enhancement in coiled-tube heat exchangers. *Int. J. Heat Mass Transf.*, 44(17):3189–3199, 2001.

[3] S. Ali. Pressure drop correlations for flow through regular helical coil tubes. *Fluid Dyn. Res.*, 28:295–310, 2001.

[4] H. Aref. Stirring by chaotic advection. *J. Fluid Mech.*, 143:1–21, 1984.

[5] H. Aref, J.R. Blake, M. Budišić, S.S.S. Cardoso, J.H.E. Cartwright, H.J.H. Clercx, K. El Omari, U. Feudel, R. Golestanian, E. Gouillart, G.F. van Heijst, T. S. Krasnopolskaya, Y. Le Guer, R.S. MacKay, V.V. Meleshko, G. Metcalfe, I. Mezić, A.P.S. de Moura, O. Piro, M.F.M. Speetjens, R. Sturman, J.-L. Thiffeault, and I. Tuval. Frontiers of chaotic advection. *Rev. Mod. Phys.*, 89:025007, 2017.

[6] K. Awasthi, D.S. Reddy, and M.K. Khan. Performance comparison among the variants of curved serpentine coil. *Phys. Fluids*, 33(7):073604, 2021.

[7] M. Bahiraei and N. Mazaheri. Second law analysis for flow of a nanofluid containing graphene–platinum nanoparticles in a minichannel enhanced with chaotic twisted perturbations. *Chem. Eng. Res. Des.*, 136:230–241, 2018.

[8] S.A. Bahrani, L. Humberset, R. Osipian, L. Royon, K. Azzouz, and A. Bontemps. How thermally efficient are chaotic advection mixers? An experimental assessment. *Int. J. Therm. Sci.*, 145:106046, 2019.

[9] B. Bara, K. Nandakumar, and J.H. Masliyah. An experimental and numerical study of the Dean problem: flow development towards two-dimensional multiple solutions. *J. Fluid Mech.*, 244:339–376, 1992.

[10] S.A. Berger, L. Talbot, and L.S. Yao. Flow in curved pipes. *Ann. Rev. Fluid Mech.*, 15: 461–512, 1983.

[11] C. Boesinger, Y. Le Guer, and M. Mory. Experimental study of reactive chaotic flows in tubular reactors. *AIChE J.*, 51:2122–2132, 2005.

[12] C. Castelain, A. Mokrani, Y. Le Guer, and H. Peerhossaini. Experimental study of chaotic advection regime in a twisted duct flow. *Eur. J. Mech. - B/Fluids*, 20(2):205–232, 2001.

[13] C. Chagny, C. Castelain, and H. Peerhossaini. Chaotic heat transfer for heat exchanger design and comparison with a regular regime for a large range of Reynolds numbers. *Appl. Therm. Eng.*, 20:1615–1648, 2000.

[14] H.C. Chang and M. Sen. Application of chaotic advection to heat transfer. *Chaos Solitons Fract.*, 4:955–976, 1994.

[15] H. Chaté, E. M. Villermaux, and J.M. Chomaz, editors. *Mixing Chaos and Turbulence*, volume 373 of *NATO ASI Series B Physics*. Kluwer Academic – Plenum Publishers, New York, 1999.

[16] K. Cieślicki and A. Piechna. Can the Dean number alone characterize flow similarity in differently bent tubes? *J. Fluids Eng.*, 134:051205, 2012.

[17] A.N. Cookson, D.J. Doorly, and S.J. Sherwin. Efficiently generating mixing by combining differing small amplitude helical geometries. *Fluids*, 4:59–84, 2019.

[18] M. Creyssels, S. Prigent, Y. Zhou, X. Jianjin, C. Nicot, and P. Carrière. Laminar heat transfer in the MLLM static mixer. *Int. J. Heat Mass Transf.*, 81:774–783, 2015.

[19] Y. Cui, W. Wang, B. Li, and D. Zuo. Numerical study on the thermal-hydraulic performance of a circular-arc-wavy helically coiled heat exchanger developed based on chaotic advection. *Int. J. Heat Mass Transf.*, 159:120084, 2020.

[20] T. Dbouk and C. Habchi. On the mixing enhancement in concentrated non-colloidal neutrally buoyant suspensions of rigid particles using helical coiled and chaotic twisted pipes: A numerical investigation. *Chem. Eng Process*, 141:107540, 2019.

[21] W.R. Dean. Note on the motion of fluid in a curved pipe. *Phil. Mag.*, 4(4):208–223, 1927.

[22] W.R. Dean. The streamline motion of fluid in a curved pipe. *Phil. Mag.*, 5(30):673–695, 1928.

[23] F. Delplace. Laminar flow of newtonian liquids in ducts of rectangular cross-section a model for both physics and mathematics. *Int. J. Math. Theor. Phys.*, 1:198–201, 2018.

[24] M.P. Do Carmo. *Differential geometry of curves and surfaces: revised and updated second edition*. Courier Dover Publications, 2016.

[25] K. El Omari and Y. Le Guer. Alternate rotating walls for thermal chaotic mixing. *Int. J. Heat Mass Transf.*, 53:123–134, 2010.

[26] MA Farajzadeh and A Tohidi. Mixing and heat transfer enhancement of power-law fluids inside helically coiled tube by chaotic advection. *J. of Non-Newton. Fluid Mech.*, 274:104202, 2019.

[27] H. Fellouah, C. Castelain, A. Ould El Moctar, and H. Peerhossaini. A criterion for detection of the onset of Dean instability in Newtonian fluids. *Eur. J. Mech. B Fluids*, 25:505–531, 2006.

[28] M.R. Gaddem, S. Ookawara, K.D.P. Nigam, S. Yoshikawa, and H. Matsumoto. Hydrodynamics and mixing in a novel design of compact microreactors: arc flow inverters. *Chem. Eng. Process.*, page 108770, 2021.

[29] D. Gammack and P.E. Hydon. Flow in pipes with non-uniform curvature and torsion. *J. Fluid Mech.*, 433:357–382, 2001.

[30] P. Garg, J.R. Picardo, and S. Pushpavanam. Chaotic mixing in a planar, curved channel using periodic slip. *Phys. Fluids*, 27(3):032004, 2015.

[31] M. Germano. On the effect of torsion on a helical pipe flow. *J. Fluid Mech.*, 125:1–8, 1982.

[32] M. Germano. The Dean equations extended to a helical pipe flow. *J. Fluid Mech.*, 203: 289–305, 1989.

[33] C. Geuzaine and J.-F. Remacle. Gmsh: a three-dimensional finite element mesh generator with built-in pre- and post-processing facilities. *Int. J. Numer. Meth. Engng*, 79:1309–1331, 2009.

[34] C. Habchi and J.-L. Harion. Residence time distribution and heat transfer in circular pipe fitted with longitudinal rectangular wings. *Int. J. of Heat Mass Transf.*, 74:13–24, 2014.

[35] C. Habchi, T. Lemenand, D. Della Valle, and H. Peerhossaini. Liquid/liquid dispersion in a chaotic advection flow. *Int. J. Multiph. Flow*, 35(6):485–497, 2009.

[36] C. Habchi, S. Ouarets, T. Lemenand, D. Della Valle, J. Bellettre, and H. Peerhossaini. Influence of viscosity ratio on droplets formation in a chaotic advection flow. *Int. J. Chem. React. Eng.*, 7:1–16, 2009.

[37] P. Hille, R. Vehrenkamp, and E.O. Schulz-Dubois. The development and structure of primary and secondary flow in a curved square duct. *J. Fluid Mech.*, 151:219–241, 1985.

[38] H. Jasak, A. Jemcov, and Z. Tuković. OpenFOAM: A C++ library for complex physics simulations. volume 1000 of *International workshop on coupled methods in numerical dynamics*, pages 1–20, 2007.

[39] M. Jokiel, N.M. Kaiser, P. Kováts, M. Mansour, K. Zähringer, K.D.P. Nigam, and K. Sundmacher. Helically coiled segmented flow tubular reactor for the hydroformylation of long-chain olefins in a thermomorphic multiphase system. *Chem. Eng. J.*, 377:120060, 2019.

[40] S.W. Jones, O.M. Thomas, and H. Aref. Chaotic advection by laminar flow in a twisted pipe. *J. Fluid Mech.*, 209:335–357, 1989.

[41] P. Kováts, D. Pohl, D. Thévenin, and K. Zähringer. Optical determination of oxygen mass transfer in a helically-coiled pipe compared to a straight horizontal tube. *Chem. Eng. Sci.*, 190:273–285, 2018.

[42] J. Kühnen, P. Braunshier, M. Schwegel, H.C. Kuhlmann, and B. Hof. Subcritical versus supercritical transition to turbulence in curved pipes. *J. Fluid Mech.*, 770:R3, 2015.

[43] V. Kumar, M. Mridha, A.K. Gupta, and K.D.P. Nigam. Coiled flow inverter as a heat exchanger. *Chem. Eng. Sci.*, 62(9):2386–2396, 2007.

[44] Y. Le Guer and H. Peerhossaini. Order breaking in Dean flow. *Phys. Fluids*, A3:1029–1032, 1991.

[45] K.E. Lee, K.H. Parker, C.G. Caro, and S.J. Sherwin. The spectral/hp element modelling of steady flow in non-planar double bends. *Int. J. Numer. Meth. Fluids*, 57(5):519–529, 2008.

[46] T. Lemenand and H. Peerhossaini. A thermal model for prediction of the Nusselt number in a pipe with chaotic flow. *Appl. Therm. Eng.*, 22(15):1717–1730, 2002.

[47] Y. Levy, D. Degani, and A. Seginer. Graphical visualization of vortical flows by means of helicity. *AIAA J.*, 28(8):1347–1352, 1990.

[48] P.M. Ligrani, J.E. Longest, M.R. Kendall, and W.A. Fields. Splitting, merging and spanwise wavenumber selection of Dean vortex pairs. *Exp. Fluids*, 18:41–58, 1994.

[49] W. Luo, H. Han, R. Yu, L. Cai, and R. Gao. Flow and heat transfer characteristics of air and n-decane in eccentric tube-in-tube helically coiled heat exchangers. *Int. J. Therm. Sci.*, 170: 107170, 2021.

[50] R.L. Manlapaz and S.W. Churchill. Fully developed laminar flow in a helically coiled tube of finite pitch. *Chem. Eng. Comm.*, 7:57–78, 1980.

[51] M. Mansour, D. Thévenin, and K. Zähringer. Numerical study of flow mixing and heat transfer in helical pipes, coiled flow inverters and a novel coiled configuration. *Chem. Eng. Sci.*, 221: 115690, 2020.

[52] P.A.J. Mees, K. Nandakumar, and J.H. Masliyah. Instability and transitions of flow in a curved square duct: the development of two pairs of Dean vortices. *J. Fluid Mech.*, 314: 227–246, 1996.

[53] A. Mokrani, C. Castelain, and H. Peerhossaini. The effects of chaotic advection on heat transfer. *Int. J. Heat Mass Transf.*, 40(13):3089–3104, 1997.

[54] F. Moukalled, L. Mangani, and M Darwish. *The Finite Volume method in Computational Fluid Dynamics - An advanced introduction with OpenFOAM and Matlab*. Springer, 2016.

[55] K. Nandakumar and J.H. Masliyah. Bifurcation in steady laminar flow through curved tubes. *J. Fluid Mech.*, 119:475–490, 1982.

[56] J.M. Ottino. *The kinematics of mixing: stretching, chaos, and transport*. Cambridge University Press, 1989.

[57] N. Ozisik. *Heat transfer: a basic approach*. Mc Graw Hill Book Co, 1985.

[58] S. Patil and P.V.V. Babu. Heat transfer augmentation in a circular tube and square duct fitted with swirl flow generators: a review. *Int. J. Chem. Eng. Appl.*, 2:326–331, 2011.

[59] H. Peerhossaini, C. Castelain, and Y. Le Guer. Heat exchanger design based on chaotic advection. *Exp. Therm. Fluid Sci.*, 7(4):333–344, 1993.

[60] L. Prandtl. Erzeugung von zirkulationen beim schütteln von gefäßen. *ZAMM Z. fur Angew. Math. Mech.*, 29(1-2):8–9, 1949.

[61] D.S. Reddy, M.K. Khan, and K. Awasthi. Thermohydraulic performance of a novel curved serpentine coil. *Phys. Fluids*, 32:083609, 2020.

[62] P.J. Roache. *Verification and validation in computational science and engineering*, volume 895. Hermosa Albuquerque, NM, 1998.

[63] M. Rousta, E. Shirani, and Z. Habibi. A comprehensive study on the characterization of chaotic advection flow and heat transfer in a twisted pipe with elliptical cross-section. *Results Eng.*, 13:100323, 2022.

[64] D.F. Schmidt. Warmeubarang and druckverlust in rohrshlangen. *Chem. Eng. Tech.*, 13: 781–789, 1967.

[65] R. Shah and A. London. Laminar flow forced convection heat transfer and flow friction in straight and curved ducts - a summary of analytical solutions. page 117, 1971.

[66] H. Shi, N. Di Miceli Raimondi, D.F. Fletcher, M. Cabassud, and C. Gourdon. Numerical study of heat transfer in square millimetric zigzag channels in the laminar flow regime. *Chem. Eng. Process.: Process Intens.*, 144:107624, 2019.

[67] M. Speetjens, G. Metcalfe, and M. Rudman. Lagrangian transport and chaotic advection in three-dimensional laminar flows. *Appl. Mech. Rev.*, 73(3), 2021.

[68] P.S. Srinivasan. Pressure drop and heat transfer in coils. *Chem. Eng.*, 218:CE113–CE119, 1968.

[69] A. Tohidi, S.M. Hosseinalipour, M. Shokrpour, and A.S. Mujumdar. Heat transfer enhancement utilizing chaotic advection in coiled tube heat exchangers. *Appl. Therm. Eng.*, 76: 185–195, 2015.

[70] S. Vashisth, V. Kumar, and K.D.P. Nigam. A review on the potential applications of curved geometries in process industry. *Ind. Eng. Chem. Res.*, 47:3291–3337, 2008.

[71] M. Wang, M. Zheng, M. Chao, J. Yu, X. Zhang, and L. Tian. Experimental and CFD estimation of single-phase heat transfer in helically coiled tubes. *Prog. Nucl. En.*, 112:185–190, 2019.

[72] K. H. Winters. A bifurcation study of laminar flow in a curved tube of rectangular cross-section. *J. Fluid Mech.*, 180:343–369, 1987.

[73] J. Wu, X. Li, H. Liu, K. Zhao, and S. Liu. Calculation method of gas–liquid two-phase boiling heat transfer in helically-coiled tube based on separated phase flow model. *Int. J. Heat Mass Transf.*, 161:120242, 2020.

[74] A. Yamagishi, T. Inaba, and Y. Yamaguchi. Chaotic analysis of mixing enhancement in steady laminar flows through multiple pipe bends. *Int. J. Heat Mass Transf.*, 50:1238–1247, 2007.

[75] L.S. Yao and S.A. Berger. Flow in heated curved pipes. *J. Fluid. Mech.*, 88:339–354, 1978.

[76] C. Zhang and K. Nandakumar. Enhancement of heat transfer in laminar flows using a toroidal helical pipe. *Ind. Eng. Chem. Res.*, 59:3922–3933, 2019.

[77] C. Zhang, A.R Ferrell, and K. Nandakumar. Study of a toroidal-helical pipe as an innovative static mixer in laminar flows. *Chem. Eng. J.*, 359:446–458, 2019.

[78] Z. Zheng, D.F. Fletcher, and B.S Haynes. Chaotic advection in steady laminar heat transfer simulations: Periodic zigzag channels with square cross-sections. *Int. J. Heat Mass Transf.*, 57(1):274–284, 2013.

[79] Z. Zheng, D.F. Fletcher, and B.S. Haynes. Laminar heat transfer simulations for periodic zigzag semicircular channels: chaotic advection and geometric effects. *Int. J. Heat Mass Transf.*, 62:391–401, 2013.

[80] Z. Zheng, A.M. Johnston, D.F. Fletcher, and B.S. Haynes. Heat exchanger specification: Coupling design and surface performance evaluation. *Chem. Eng. Res. Des.*, 93:392–401, 2015.